

STRIP THE STRIPES: ARTIFACT DETECTION AND REMOVAL FOR SCANNING ELECTRON MICROSCOPY IMAGING

Amirhossein Khalilian-Gourtani^{*†} Mariano Tepper[†] Victor Minden[†] Dmitri B. Chklovskii^{†‡}

^{*}Electrical and Computer Engineering Department, New York University, Brooklyn, NY 11201

[†]Center for Computational Biology, Flatiron Institute, New York, NY 10010

[‡]Neuroscience Institute, NYU Langone Medical Center, New York, NY 10016

ABSTRACT

Scanning Electron Microscopy (SEM) is a popular high resolution imaging modality for biological samples that has recently been applied to neural circuit reconstruction. For this application, relatively large volumes are imaged by repeatedly ablating away the exposed surface of the volume with a focused ion beam (FIB), which can cause beam-aligned striping artifacts in images of the remaining layers. We present an automatic pipeline designed to detect and correct for such striping artifacts while minimally degrading the unknown artifact-free image. The proposed method addresses this problem by computing a data-driven mask for the corrupted frequency band and subsequently solving a variational formulation of the image reconstruction problem using efficient methods from convex optimization. Results on simulated and real data show state-of-the-art denoising performance.

Index Terms— stripe-artifacts removal, total variation, non-linear filtering, scanning electron microscopy.

1. INTRODUCTION

Originally developed for materials science research, Focused Ion Beam Scanning Electron Microscopy (FIB-SEM) has been used in recent years to probe biological structures. The isotropic spatial resolution achieved by FIB-SEM (nanometers) makes it the imaging modality of choice used for the reconstruction of insect neural circuit (connectomics) [1]. In this imaging technique, a sequence of ablations of the fine layer of material using a focused ion beam alternates with an electron microscopy step to image the newly exposed surface. Although the ion beam allows for fine cuts of the surface leading to high z-resolution, it leaves unidirectional striping artifacts by carrying heavy metal atoms down the surface, Fig. 1(a). The effectiveness of the machine learning techniques for segmentation of the FIB-SEM images is greatly reduced when such artifact is present. Additionally, these artifacts can be severe and may create images incomprehensible for human annotators.

There are many different methods for stripe removal. Examples range from using simple filtering techniques to remove the affected frequency band of the images [2] to combining wavelet and Fourier filtering techniques to exploit the unidirectional structure of the stripes [3, 4]. However, these techniques require the design of precise hand-crafted filters and do not utilize the properties of the underlying image. Related popular methods for denoising with structured noise also utilize curvelets and shearlets [5, 6] and dictionary learning [7]. Another approach, used in geoscience and remote sensing applications, is to formulate and solve an ill-posed inverse problem [8]. Methods in this family assume a low-rank prior on the structure of the stripes and utilize low-rank and sparse decomposition techniques. However, the low-rank assumption only holds

when the stripes cover the entire field of view, which is not the case in FIB-SEM imaging.

Our goal in this work is to leverage signal processing techniques to correct the striping artifacts in FIB-SEM images while keeping the true underlying structures (approximately) intact. The proposed pipeline utilizes the properties of the stripes in the Fourier domain to automatically detect the corrupted frequency band (Sec. 2.1). The proposed framework then admits different variational formulations of the inverse problem allowing for a trade-off between speed and simplicity of the method on one hand and accuracy on the other (Sec. 2.2). Additionally, the proposed methods take both frequency and image domain properties of the data into account. Results on simulated and real data show state-of-the-art denoising performance (Sec. 3). Although this study focuses on FIB-SEM, the developed framework is general and can be easily extended to other imaging modalities.

2. PROBLEM FORMULATION AND SOLUTION

Given N_d image “slices” and supposing each two-dimensional (2D) slice image is of size $N_h \times N_v$, we formally model the observed volumetric image $\mathbf{Y} \in [0, 1]^{N_h \times N_v \times N_d}$ by decomposing it as

$$\mathbf{Y} = \mathbf{Z} + \mathbf{B} + \mathbf{N} \quad (1)$$

where \mathbf{Z} , \mathbf{B} , and \mathbf{N} are the (unknown) true underlying image, additive stripe artifacts, and additive standard Gaussian noise, respectively. Based on the data (Fig. 1(a)) we assume that the underlying image \mathbf{Z} is locally smooth with sparse gradient, and that its edges have no strong direction preference such that the image may be considered in a sense isotropic. We also assume that the stripes in \mathbf{B} are unidirectional with preferred direction in the xy -plane, though each stripe need not necessarily span the entire image. Additionally, we assume that each stripe is smooth in the longitudinal direction. Our goal is to recover \mathbf{Z} given only \mathbf{Y} , which we accomplish by first detecting a mask that roughly isolates the stripes \mathbf{B} in Fourier space and then solving a variational image reconstruction problem based either on annihilating corrupted frequency bands (simple and fast) or on solving a convex optimization problem (high accuracy) depending on application demands.

2.1. Detecting corrupted frequency coefficients

As the stripes are unidirectional, most of the spectral energy of \mathbf{B} is contained in a narrow frequency band perpendicular to the direction of the stripes (e.g., for vertical stripes as in Fig. 1(a), most of the frequency content is near the horizontal axis as in Fig. 1(b)). This motivates our approach for detecting the corrupted frequencies of the image. Taking the 2D Fourier transform of each slice of \mathbf{Y} , we

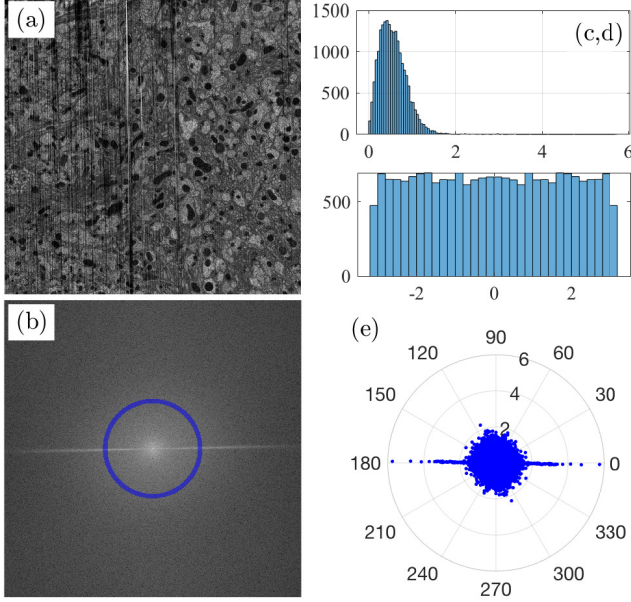


Fig. 1: (a) A noisy image (b) its FFT with a single annulus highlighted in blue. (c,d) Histograms of magnitude and phase of the coefficients in \mathcal{A}_r ; we can empirically observe that they follow Rayleigh and uniform distributions, respectively. (e) Scatter plot of coefficient magnitudes versus polar angle on the annulus.

denote the result as $\hat{\mathbf{Y}} \triangleq \mathcal{F}_2 \mathbf{Y} \in \mathbb{C}^{N_h \times N_v \times N_d}$ with slices $\hat{\mathbf{Y}}_k \in \mathbb{C}^{N_h \times N_v}$. With this, the proposed framework computes a data-driven binary mask $\Omega \in \{0, 1\}^{N_h \times N_v \times N_d}$ (where $\Omega_{ijk} = 1$ indicates that the corresponding Fourier coefficient $\hat{\mathbf{Y}}_{ijk}$ is likely corrupted by the stripes) as follows.

In contrast to the unidirectional stripes, the image is assumed isotropic, so it is natural to consider the image statistics on an annular domain in frequency space. For each slice k , we begin by covering the frequency domain of $\hat{\mathbf{Y}}_k$ with non-overlapping thin concentric annuli. Let \mathcal{A}_r^k be Fourier coefficients in a thin annulus of radius r and width δ centered at the frequency origin (i_0, j_0, k) ,

$$\mathcal{A}_r^k = \left\{ \hat{\mathbf{Y}}_{(x+i_0)(y+j_0)k} \mid (r-\delta)^2 \leq x^2 + y^2 \leq (r+\delta)^2 \right\}. \quad (2)$$

Except in the corrupted band, the coefficients in each \mathcal{A}_r^k (except in the small corrupted band) empirically follow a 2D Gaussian distribution with parameters μ and Σ that can be robustly estimated using standard methods. We whiten each element $a_{ijk} \in \mathcal{A}_r^k$ by subtracting the mean and multiplying it by the precision matrix, denoting the result as $\tilde{a}_{ijk} \in \tilde{\mathcal{A}}_r^k$.

After whitening, the magnitude of these complex numbers therefore follows a standard Rayleigh distribution. As an example, Fig. 1(b,c,d) show a sample annulus and histograms of the magnitude and phase of the Fourier coefficients in it. In Fig. 1(e), we take each coefficient in the annulus and give a polar plot of its magnitude versus its angle along the ring, which shows that corrupted coefficients have higher magnitude and do not follow the estimated Gaussian distribution. As a result, the tail of the corresponding Rayleigh distribution provides a reliable test measure for the hypothesis that any given coefficient in $\tilde{\mathcal{A}}_r^k$ follows the Gaussian distribution and hence, is not corrupted. Then, we form an outliers map P using the test

$$P_{ijk} = \left\{ \mathbf{1}_{[S(|\tilde{a}_{ijk}|) \leq \epsilon]} \mid \tilde{a}_{ijk} \in \tilde{\mathcal{A}}_r^k \right\}, \quad (3)$$

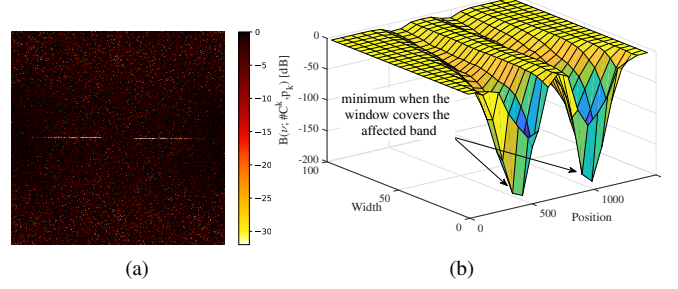


Fig. 2: (a) p -values (in log-scale) from survival function of the Rayleigh distribution, see Eq. (3). (b) Probabilities from Eq. (6) for boxes/rectangles of different sizes.

Alg. 1: Frequency Mask Detection

```

1 Input:  $\mathbf{Y}$  and  $\epsilon$ ;
2 for  $k = 1, \dots, N_d$  do
3    $\hat{\mathbf{Y}}_k \leftarrow \mathcal{F}_2 \mathbf{Y}_k$ ;
4   Populate the outliers map  $P$  using eqs. (2) and (3);
5    $\theta_{\min} \leftarrow \arg \min_{\theta} \mathcal{B}(\#\{c = 1 \mid c \in \mathcal{C}_{\theta}^k\}; \#\mathcal{C}_{\theta}^k, p_k)$ ;
6    $P \leftarrow \text{rotate}(P, -\theta_{\min})$ ;
7    $B_{\min} \leftarrow \arg \min_B \mathcal{B}(\#\{c = 1 \mid c \in \mathcal{C}_B^k\}; \#\mathcal{C}_B^k, p_k)$ ;
8   for  $(i, j) \in B_{\min}$  do  $\Omega(i, j, k) \leftarrow 1$ ;
9 Output:  $\theta_{\min}, \Omega$ ;
```

where $S(x) = \exp(-x^2/2)$ is the survival function of the standard Rayleigh distribution. $P_{ijk} = 1$ indicates that the Fourier coefficient at position ij in slice k is an outlier with respect to our Gaussian assumption. Fig. 2(a) shows the p -values for a slice.

The distribution of the p -values in the corrupted region is different than other sub-regions. Let θ be an orientation and B be a rectangle within the slice. We then define sets

$$\mathcal{C}_{\theta}^k = \{P_{ijk} \mid i \cos \theta + j \sin \theta = 0\}, \quad (4)$$

$$\mathcal{C}_B^k = \{P_{ijk} \mid B_{\text{top}} \leq i \leq B_{\text{bottom}} \wedge B_{\text{left}} \leq j \leq B_{\text{right}}\}. \quad (5)$$

We can test whether the number of outliers in a given subset \mathcal{C}^k (which can be either a box or an orientation) of P is surprisingly high compared with the total number of outliers in P . We perform that test using the probability

$$\mathcal{B}(\#\{c = 1 \mid c \in \mathcal{C}^k\}; \#\mathcal{C}^k, p_k), \quad (6)$$

where $p_k = \sum_{ij} P_{ijk} / (N_h \cdot N_v)$ and \mathcal{B} indicates the tail of the binomial distribution.

The detection procedure, presented in Alg. 1, works as follows. We first use Eq. (3) to create an outliers map. We detect the orientation for which we observe maximal deviation from the null hypothesis. We then rotate the outliers map so that the maximal deviation is now aligned with the horizontal axis. Then we repeat the maximal deviation test using boxes. The selected box provides the region where the Fourier coefficients maximally deviate from the Gaussian assumption.

Note that we could use Eq. (6) to test whether the slice is corrupted with stripe-artifacts by setting a threshold on the probability. When we know that the images are indeed corrupted, as is the case of this work, we omit such test.

Alg. 2: Dykstra's projection algorithm applied to Eq. (7)

```

1 Input:  $\mathbf{Y}$  and  $\Omega$ ;
2  $\hat{\mathbf{Z}} \leftarrow \mathcal{F}_2 \mathbf{Y}$ ;  $\mathbf{U}_\Omega \leftarrow \mathbf{0}$ ;  $\mathbf{U}_\ell \leftarrow \mathbf{0}$ ;
3 while not converged do
4    $\mathbf{Z} \leftarrow \mathcal{F}_2^{-1} \mathcal{P}_\Omega (\hat{\mathbf{Z}} + \mathbf{U}_\Omega)$ ;
5    $\mathbf{U}_\Omega \leftarrow \hat{\mathbf{Z}} + \mathbf{U}_\Omega - \mathcal{P}_\Omega (\hat{\mathbf{Z}} + \mathbf{U}_\Omega)$ ;
6    $\hat{\mathbf{Z}} \leftarrow \mathcal{F}_2 \mathcal{P}_{[0,1]} (\mathbf{Z} + \mathbf{U}_\ell)$ ;
   //  $\mathcal{P}_{[0,1]}$  is a clipping operator
7    $\mathbf{U}_\ell \leftarrow \mathbf{Z} + \mathbf{U}_\ell - \mathcal{P}_{[0,1]} (\mathbf{Z} + \mathbf{U}_\ell)$ ;
8 Output:  $\mathbf{Z}_{\text{est}} = \mathbf{Z}$ ;
```

2.2. De-stripping as an inverse problem

We can estimate \mathbf{Z} in Eq. (1) by solving an inverse problem using the detected mask and the prior assumptions. Directly annihilating the corrupted frequency band would produce an estimate with pixel values outside the desired range. Intuitively, the desired result should be similar to the noisy image outside the corrupted frequency band, should be zero inside the corrupted frequency band, and its values should be in the range $[0, 1]$. We thus solve the minimization problem

$$\mathbf{Z}_{\text{est}} = \arg \min_{\mathbf{Z}} \|\mathbf{Z} - \mathbf{Y}\|_F^2 \quad \text{s.t.} \quad \begin{aligned} &\mathcal{P}_\Omega (\mathcal{F}_2 \mathbf{Z}) = \mathbf{0}, \\ &\mathbf{Z}_{ij} \in [0, 1] \quad \forall i, j, \end{aligned} \quad (7)$$

where the projection operator $\mathcal{P}_\Omega(\cdot)$ sets to zero the values inside the frequency mask Ω (found in the previous section). The solution to Eq. (7) can be obtained by applying Dykstra's projection algorithm [9], which finds the closest point to the initial point, \mathbf{Y} , in the intersection of both convex sets. The details of the method are provided in Algorithm 2. We name the mask detection followed by Alg. 2 **FFT-RingV1**.

An alternative approach that makes better use of the image properties is the following formulation. It is desired that the output image be similar to the underlying structure, have the same range of values, and match the noisy image outside the corrupted frequency band. Following our assumptions in Sec. 2, we also enforce sparsity of the image gradient and longitudinal smoothness of the stripes (we assume that they are vertical as we can use θ_{\min} from Alg. 1 to rotate the images). Formally,

$$\begin{aligned} \min_{\mathbf{Z}} & \underbrace{\|\Omega^c \circ (\alpha \mathcal{F}_2 \mathbf{Z} - \mathcal{F}_2 \mathbf{Y})\|_F^2}_{\text{data fidelity outside the mask}} + \underbrace{\lambda_x \|\mathbf{DZ}\|_1}_{\text{local smoothness}} \\ & + \underbrace{\lambda_z \|\mathbf{L}_v(\mathbf{Z} - \mathbf{Y})\|_F^2}_{\text{second order vertical changes}} + \underbrace{\sum_{i,j,k} \iota_{[0,1]}(\mathbf{Z}_{ijk})}_{\text{keep pixels in range}}, \end{aligned} \quad (8)$$

where: $\|\mathbf{DZ}\|_1 = \sum_{i,j,k} ((\mathbf{D}_h \mathbf{Z})_{ijk}^2 + (\mathbf{D}_v \mathbf{Z})_{ijk}^2 + (\mathbf{D}_d \mathbf{Z})_{ijk}^2)^{1/2}$ with $\mathbf{D}_h, \mathbf{D}_v, \mathbf{D}_d$ being the horizontal, vertical, and depth derivative operators, respectively [10]; \mathbf{L}_v is the vertical Laplacian, i.e., second derivative in the vertical direction only; \circ denotes the entry-wise product; Ω^c is the complement of the detected frequency mask, formed by stacking the individual 2D masks; and $\iota_C(\cdot)$ is the indicator function of the convex set C [9]. Additionally, λ_x and λ_z parameterize the amount of regularization and therefore control the trade-off between smoothing and stripe removal. Parameters are tuned using grid search over a reasonable set of values and validated using cross-validation. Parameter α scales the frequency domain variables

Alg. 3: ADMM applied to Eq. (9)

```

1 Input:  $\mathbf{Y}, \Omega^c, \lambda_x, \lambda_z, \rho_1, \rho_2, \rho_3, \alpha$ ;
2  $\hat{\mathbf{Y}} \leftarrow \mathcal{F}_2 \mathbf{Y}$ ;  $\mathbf{X} \leftarrow \mathbf{D}\mathbf{Y}$ ;  $\mathbf{Z} \leftarrow \mathbf{Y}$ ;  $\tilde{\mathbf{Z}} \leftarrow \mathbf{Y}$ ;
3  $\tilde{\mathbf{Z}} \leftarrow \mathcal{F}_2 \mathbf{Y}$ ;  $\mathbf{U}_{Z_i} \leftarrow \mathbf{0}$ ;  $\mathbf{U}_X \leftarrow \mathbf{0}$ ;  $\tilde{\mathbf{U}} \leftarrow \mathbf{0}$ ;
4 while not converged do
   //Main operations detailed in comments
5    $\hat{\mathbf{Z}} \leftarrow \arg \min_{\mathbf{A}} \mathcal{L}(\mathbf{A}, \tilde{\mathbf{Z}}, \mathbf{Z}, \mathbf{X})$ ; //diag. syst. solve
6    $\tilde{\mathbf{Z}} \leftarrow \arg \min_{\mathbf{A}} \mathcal{L}(\tilde{\mathbf{Z}}, \mathbf{A}, \mathbf{Z}, \mathbf{X})$ ; //diag. syst. solve
7    $\mathbf{Z} \leftarrow \arg \min_{\mathbf{A}} \mathcal{L}(\hat{\mathbf{Z}}, \tilde{\mathbf{Z}}, \mathbf{A}, \mathbf{X})$ ; //element clipping
8    $\mathbf{X} \leftarrow \arg \min_{\mathbf{A}} \mathcal{L}(\hat{\mathbf{Z}}, \tilde{\mathbf{Z}}, \mathbf{Z}, \mathbf{A})$ ; //soft-thresholding
9    $\mathbf{U}_X \leftarrow \mathbf{U}_X - \mathbf{D}\tilde{\mathbf{Z}}$ ;
10   $\mathbf{U}_Z \leftarrow \mathbf{U}_Z + \mathbf{Z} - \mathcal{F}_2^{-1}(\alpha \hat{\mathbf{Z}})$ ;
11   $\tilde{\mathbf{U}} \leftarrow \tilde{\mathbf{U}} + \mathbf{Z} - \tilde{\mathbf{Z}}$ ;
12 Output:  $\mathbf{Z}$ ;
```

to the order of image domain ones. The problem is convex and the solution can be obtained using a splitting method such as Alternating Direction Method of Multipliers (ADMM) [9, 11]. Eq. (8) can be rewritten as

$$\begin{aligned} \min_{\tilde{\mathbf{Z}}, \mathbf{X}, \mathbf{Z}, \tilde{\mathbf{Z}}} & \left\| \Omega^c \circ (\alpha \hat{\mathbf{Z}} - \hat{\mathbf{Y}}) \right\|_F^2 + \lambda_x \|\mathbf{X}\|_1 \\ & + \lambda_z \left\| \mathbf{L}_v(\tilde{\mathbf{Z}} - \mathbf{Y}) \right\|_F^2 + \sum_{i,j,k} \iota_{[0,1]}(\mathbf{Z}_{ijk}) \\ \text{s.t.} & \quad \alpha \mathcal{F}_2^{-1} \hat{\mathbf{Z}} = \mathbf{Z}, \quad \mathbf{D}\tilde{\mathbf{Z}} = \mathbf{X}, \quad \tilde{\mathbf{Z}} = \mathbf{Z}. \end{aligned} \quad (9)$$

The equality constraints are removed by introducing the ADMM dual variables $\mathbf{U}_Z, \mathbf{U}_X$, and $\tilde{\mathbf{U}}$ and forming the scaled augmented Lagrangian,

$$\begin{aligned} \mathcal{L}(\hat{\mathbf{Z}}, \tilde{\mathbf{Z}}, \mathbf{Z}, \mathbf{X}) &= \left\| \Omega^c \circ (\alpha \hat{\mathbf{Z}} - \hat{\mathbf{Y}}) \right\|_F^2 + \lambda_x \|\mathbf{X}\|_1 \\ &+ \sum_{i,j,k} \iota_{[0,1]}(\mathbf{Z}_{ijk}) + \lambda_z \left\| \mathbf{L}_v(\tilde{\mathbf{Z}} - \mathbf{Y}) \right\|_F^2 \\ &+ \frac{\rho_1}{2} \left\| \alpha \mathcal{F}_2^{-1} \hat{\mathbf{Z}} - \mathbf{Z} + \mathbf{U}_Z \right\|_F^2 \\ &+ \frac{\rho_2}{2} \left\| \mathbf{D}\tilde{\mathbf{Z}} - \mathbf{X} + \mathbf{U}_X \right\|_F^2 \\ &+ \frac{\rho_3}{2} \left\| \tilde{\mathbf{Z}} - \mathbf{Z} + \tilde{\mathbf{U}} \right\|_F^2. \end{aligned} \quad (10)$$

The algorithm iteratively minimizes the augmented Lagrangian with respect to each variable and updates the duals, see Algorithm 3. We name the mask detection followed by Alg. 3 **FFT-RingV2**. Note that each sub-problem can be solved very efficiently in closed-form. The first two sub-problems involve solving linear systems of equations, efficiently done using element-wise operations. Additionally, the sub-problem involving the total variation term is solved via element-wise vector soft-thresholding [10].

3. EXPERIMENTAL RESULTS

Synthetic experiments. In this section, the proposed methods are compared to some existing ones in the literature. In order to simulate the stripping noise, an anisotropic Gabor filter at different lo-

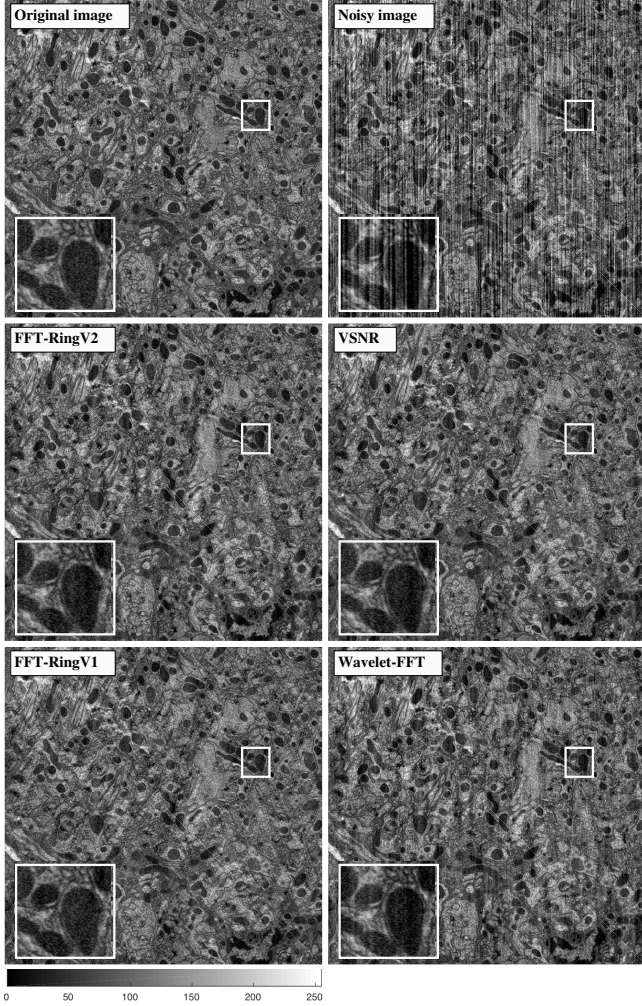


Fig. 3: Visual Results of different algorithms.

cations is used as in previous literature [12, 13]. In addition to satisfying the desired properties, this noise model allows for comparison with the Variational Stationary Noise Remover (VSNR) [12] and wavelet-FFT [3] methods. The Gabor function convolved with a simulated Bernoulli process forms the stripe artifacts. The simulated artifact is added to a clean region of the dataset. For the wavelet-FFT method five levels of Daubechies-42 filters were used. Table 1 shows the calculated peak signal-to-noise ratio (PSNR) values for different methods averaged over 30 trials leveraging different instances of simulated noises and clean images from FIB-SEM dataset.

As results in Fig. 3 and Table 1 show, FFT-RingV1 as in Eq. (7), performs similarly to the filtering approach and outperforms the wavelet-FFT method. FFT-RingV2, Eq. (8), outperforms all the methods by visual and numerical measures.

FIB-SEM images. In this section we present results of the proposed framework for the artifacts in actual FIB-SEM dataset. In a real-world scenario, variations of the artifact throughout the cube make other approaches inapplicable and the frequency detection crucial to the recovery process. A single slice of the noisy block and corresponding denoised images using both developed methods are shown in Fig. 4. These results are obtained by detecting the Fourier domain mask for each slice of a 3D cube of data and applying the image reconstruction methods. Parameters are tuned by grid search across a set of reasonable values and confirmed by cross-validation. For

Table 1: PSNR (mean \pm std) [dB] for different methods applied to images contaminated with synthetic striping artifacts. $\text{PSNR} \triangleq \max(\mathbf{Z}_{\text{est}})^2 / \|\mathbf{Z} - \mathbf{Z}_{\text{est}}\|_F$.

wavelet-FFT	FFT-RingV1	VSNR	FFT-RingV2
24.6 ± 0.3	25.55 ± 0.2	25.7 ± 0.2	26 ± 0.16

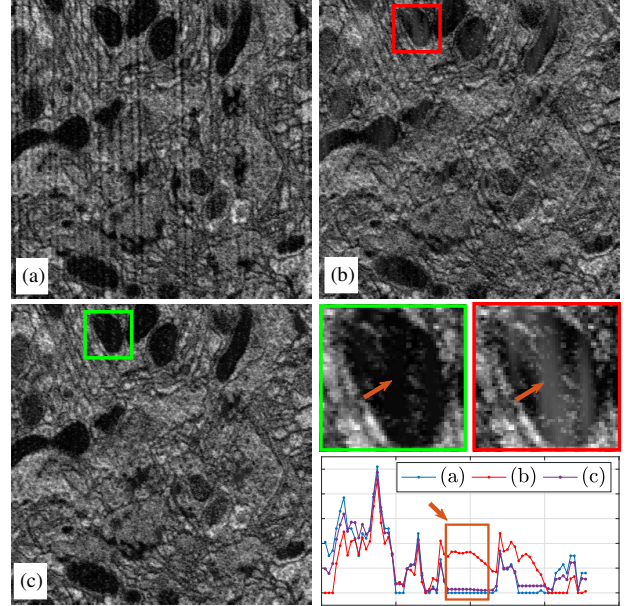


Fig. 4: One slice of (a) noisy, (b) denoised with FFT-RingV1, and (c) denoised with FFT-RingV2. In the lower right, we show zoomed regions and one horizontal scan line of each zoomed image. Better matching to the dark region.

these results, $\epsilon = 10^{-3}$, $\lambda_x = 1^{-2}$, $\alpha = 10^7$ and $\lambda_z = 10^{-1}$ were used. As shown in Fig. 4, FFT-RingV2 has better recovery results when the stripes are passing through a dark region.

4. CONCLUSION

In this study we proposed two methods for removing striping artifacts from the FIB-SEM images. The proposed pipeline leverages the frequency domain properties of the artifacts to detect the corrupted band. A simple and fast solution is obtained by annihilating the corrupted band while keeping the range of values in the image domain intact. This approach yields results of good quality. If superior quality is needed, we presented an alternative inverse problem that uses the image properties exhaustively, both in the image and frequency domains. These proposed methods, when applied to simulated and real data, showed successful results that outperform other approaches both in visual and numerical measures.

In future work, we aim to use the developed framework to help connectomics research achieve better recovery of neural circuits by introducing it into the image segmentation pipeline and as a pre-processing tool for human annotators. Additionally, the proposed methods for mask detection and associated inverse problem could be applied to other imaging modalities. Finally, we wish to explore the use of non-convex penalty terms in the inverse problems, which have shown to be successful in other applications.

Acknowledgments. We thank Anastasya Makarova and Alexey Polilov for preparing the specimen and Song Pang, Shan Xu, and Harald Hess for electron microscopy.

5. REFERENCES

- [1] C Shan Xu, Kenneth J Hayworth, Zhiyuan Lu, Patricia Grob, Ahmed M Hassan, Jose G Garcia-Cerdan, Krishna K Niyogi, Eva Nogales, Richard J Weinberg, and Harald F Hess, “Enhanced FIB-SEM systems for large-volume 3D imaging,” *Elife*, vol. 6, pp. e25916, 2017.
- [2] Jinsong Chen, Yun Shao, Huadong Guo, Weiming Wang, and Boqin Zhu, “Destriping CMODIS data by power filtering,” *IEEE Transactions on Geoscience and Remote Sensing*, vol. 41, no. 9, pp. 2119–2124, 2003.
- [3] Beat Münch, Pavel Trtik, Federica Marone, and Marco Stamparoni, “Stripe and ring artifact removal with combined wavelet—Fourier filtering,” *Optics Express*, vol. 17, no. 10, pp. 8567–8591, 2009.
- [4] Roshan Pande-Chhetri and Amr Abd-Elrahman, “De-striping hyperspectral imagery using wavelet transform and adaptive frequency domain filtering,” *ISPRS Journal of Photogrammetry and Remote Sensing*, vol. 66, no. 5, pp. 620–636, 2011.
- [5] Emmanuel Candes, Laurent Demanet, David Donoho, and Lexing Ying, “Fast discrete curvelet transforms,” *Multiscale Modeling & Simulation*, vol. 5, no. 3, pp. 861–899, 2006.
- [6] Gitta Kutyniok and Demetrio Labate, *Shearlets: Multiscale analysis for multivariate data*, Springer Science & Business Media, 2012.
- [7] Ling Shao, Ruomei Yan, Xuelong Li, and Yan Liu, “From heuristic optimization to dictionary learning: A review and comprehensive comparison of image denoising algorithms,” *IEEE Transactions on Cybernetics*, vol. 44, no. 7, pp. 1001–1013, 2014.
- [8] Yi Chang, Luxin Yan, Tao Wu, and Sheng Zhong, “Remote sensing image stripe noise removal: From image decomposition perspective,” *IEEE Transactions on Geoscience and Remote Sensing*, vol. 54, no. 12, pp. 7018–7031, 2016.
- [9] Patrick L Combettes and Jean-Christophe Pesquet, “Proximal splitting methods in signal processing,” in *Fixed-point algorithms for inverse problems in science and engineering*, pp. 185–212. Springer, 2011.
- [10] Michael K Ng, Pierre Weiss, and Xiaoming Yuan, “Solving constrained total-variation image restoration and reconstruction problems via alternating direction methods,” *SIAM Journal on Scientific Computing*, vol. 32, no. 5, pp. 2710–2736, 2010.
- [11] Stephen Boyd, Neal Parikh, Eric Chu, Borja Peleato, Jonathan Eckstein, et al., “Distributed optimization and statistical learning via the alternating direction method of multipliers,” *Foundations and Trends in Machine learning*, vol. 3, no. 1, pp. 1–122, 2011.
- [12] Jérôme Fehrenbach, Pierre Weiss, and Corinne Lorenzo, “Variational algorithms to remove stationary noise: applications to microscopy imaging,” *IEEE Transactions on Image Processing*, vol. 21, no. 10, pp. 4420–4430, 2012.
- [13] Xiao Liang, Yali Zang, Di Dong, Liwen Zhang, Mengjie Fang, Xin Yang, Alicia Arranz, Jorge Ripoll, Hui Hui, and Jie Tian, “Stripe artifact elimination based on nonsubsampling contourlet transform for light sheet fluorescence microscopy,” *Journal of Biomedical Optics*, vol. 21, no. 10, pp. 106005, 2016.